Rare Metal Materials and Engineering
Volume 55, Issue 7, July 2026
Available online at www.rmme.ac.cn

Science Press

Cite this article as: Tang Huiyi, Luan Baifeng, Zhang Fuen, et al. Hot Deformation Behavior and Microstructure Evolution of Platinum[J]. Rare Metal Materials and Engineering, 2026, 55(07): 1673-1682. DOI: https://doi.org/10.12442/j.issn.1002-185X.20250381.

ARTICLE

Hot Deformation Behavior and Microstructure Evolution of Platinum

Tang Huiyi[1,2,3], Luan Baifeng[1], Zhang Fuen[1], Xiao Yuchen[2,3], Chai Linjiang[4], Wu Baoan[2,3]

[1] International Joint Laboratory for Light Alloys (Ministry of Education), College of Materials Science and Engineering, Chongqing University, Chongqing 400045, China; [2] Chongqing Materials Research Institute Co., Ltd, Chongqing 400707, China; [3] National Engineering Research Center for Instrument Functional Materials, Chongqing 400707, China; [4] College of Materials Science and Engineering, Chongqing University of Technology, Chongqing 400054, China

Abstract: The hot deformation behavior of platinum was investigated through hot compression experiments. A constitutive equation for the prediction of the flow behavior of platinum was derived from analysis of stress-strain curves. Using the constitutive equation, the peak stress of platinum during hot working was calculated across varying temperatures and strain rates. Results show that the predicted values have strong agreement with experimental results. Electron backscatter diffraction analysis further reveals the thermal deformation mechanisms under distinct conditions within the safe processing region. The optimal processing parameters are identified as deformation temperatures of 860–910 K and strain rates of 0.01–0.1 s^{-1}. Discontinuous yielding observed at elevated strain rates is attributed to the multiplication and movement of the mobile dislocations at grain boundaries.

Key words: platinum; microstructure evolution; hot deformation; processing maps; strain rate

1 Introduction

Platinum (Pt) is widely used as high-temperature structural materials due to its high melting point (1769 ℃) and exceptional chemical stability[1]. Pt and its alloys also play a significant role in the fields of electronics and precision component manufacturing, owing to their outstanding physical and chemical properties[2]. The good ductility and fine corrosion resistance of Pt enable the Pt-based materials to undergo stretching or compression to form complex parts during processing[3]. However, its favorable ductility can paradoxically accelerate tool wear during cutting operations, while localized heat generation may induce recrystallization, posing significant challenges in the processing of Pt. During the hot deformation process, the microstructure evolution of Pt is influenced by various factors, including temperature and strain rate[4]. At elevated temperatures, the Pt-based materials of face-centered cubic crystal structure undergoes subtle transformations, which alter material properties through the variation of dislocation density, grain size, and phase structure[5]. These changes directly influence the mechanical performance and stability of Pt and its alloys. A comprehensive understanding of the hot deformation behavior of Pt and its alloys is essential for optimizing the processing techniques and enhancing their functional efficacy in practical applications[6]. Researchers have established Arrhenius-type constitutive equations and processing maps to identify the stable and unstable regions, providing guidance for the industrial production[7]. Processing maps elucidate the relationship between process parameters and microstructure, which is beneficial to the parameter selection for grain refinement and texture weakening[8]. Recent advancements integrating computational simulations with experimental studies have provided novel insights into the microstructure evolution mechanisms of Pt under different processing conditions[9]. Despite progress in Pt processing research, the investigations on microstructure evolution are rare. Particularly, the microstructure evolution of Pt under different

Received date: June 22, 2025
Foundation item: Open Fund Project of Chongqing Institute of Materials Co., Ltd (CMRI-KFJJ-202401)
Corresponding author: Luan Baifeng, Ph. D., Professor, International Joint Laboratory for Light Alloys (Ministry of Education), College of Materials Science and Engineering, Chongqing University, Chongqing 400045, P. R. China, E-mail: bfluan@cqu. edu. cn; Wu Baoan, Master, Professor, Chongqing Materials Research Institute Co., Ltd, Chongqing 400707, P. R. China, E-mail: wubaoan@163.com

temperatures and strain rates is barely studied. Besides, although the hot deformation behavior of Pt alloys has been rarely researched, the mechanism of microstructure evolution is obscure.

This study investigated the mechanical properties, hot working diagram characteristics, and microstructure evolution of Pt during hot compression, providing a foundational framework for advancing the Pt processing techniques.

2 Experiment

The Pt material used in this study was supplied by the Chongqing Institute of Material, China. Cylindrical samples (Φ8 mm×10 mm) were machined from a Pt rod through electrospray sintering technique for isothermal compression testing. Hot compression experiments were performed on a Gleeble-3500 thermal simulation tester. The schematic diagram of the hot compression test is illustrated in Fig. 1a. The samples were heated to target temperatures at a heating rate of 10 K/min and held isothermally for 5 min to ensure thermal homogeneity before compression deformation. Tests were performed at temperatures of 773, 823, 873, 923, and 973 K with strain rates of 0.01, 0.1, 1, and 10 s^{-1}, reaching a true stain of 90% (corresponding to the engineering strain of 60%). After compressive deformation was completed, each sample was immediately quenched in water and cooled to room temperature to preserve their high-temperature microstructures. Flow stress curves recorded during these experiments were not adjusted for friction or temperature effects.

To evaluate the influence of processing parameters on the microstructure of Pt, the compressed samples were cut along the compression axis, and progressively finer silicon carbide sandpaper was used to polish the exposed cross section of samples. Severe microstructural deformation and large strain accommodation occurred predominantly in the central region of the cross section, where friction effects were comparatively minimal. The sample cutting position and sample observation direction are shown in Fig.1b. The compression axial direction (AD) and radial directions (RD1 and RD2) of the extruded rod are also defined in Fig. 1b. Samples for electron backscatter diffraction (EBSD) analysis were prepared using standard mechanical polishing, followed by shock polishing for a final finish. Microstructure characterization was performed using an FEI Apreo 2S field emission scanning electron microscope (SEM) equipped with an EBSD detector. The compressed samples were cut parallel to the compression axis along the centerline for EBSD examination. After the collection of EBSD data, detailed analysis was performed using HKL Channel 5 software. The dynamic recrystallization (DRX) grains and deformed microstructures were identified by a grain orientation spread (GOS) threshold of 2°[10].

3 Results and Discussion

3.1 Materials

The Pt is in the annealed state before hot compression deformation, and its EBSD results are depicted in Fig. 2. Inverse pole figures (IPFs) of Pt along different directions are also used for analysis.

Before hot compression, the annealed Pt exhibits equiaxed grain morphology (Fig. 2a) with a coarse-grain structure, and the grain size is 155.11 μm in average. Fig. 2b reveals a pronounced <001> crystallographic texture along RD1, which

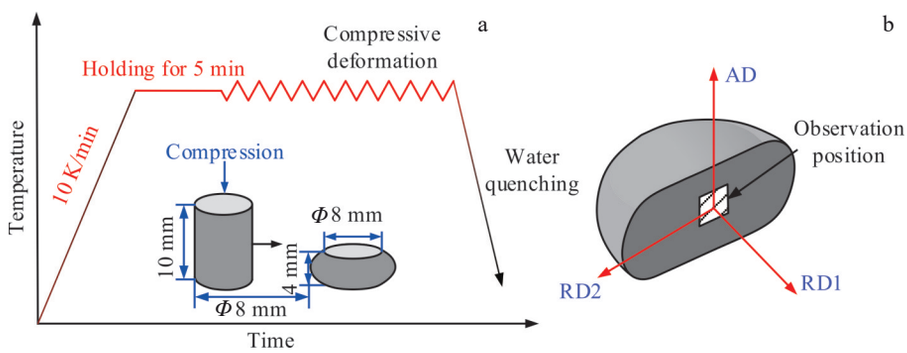

Fig.1 Schematic diagrams of hot compression test (a) and subareas and observation position on sample section (b)

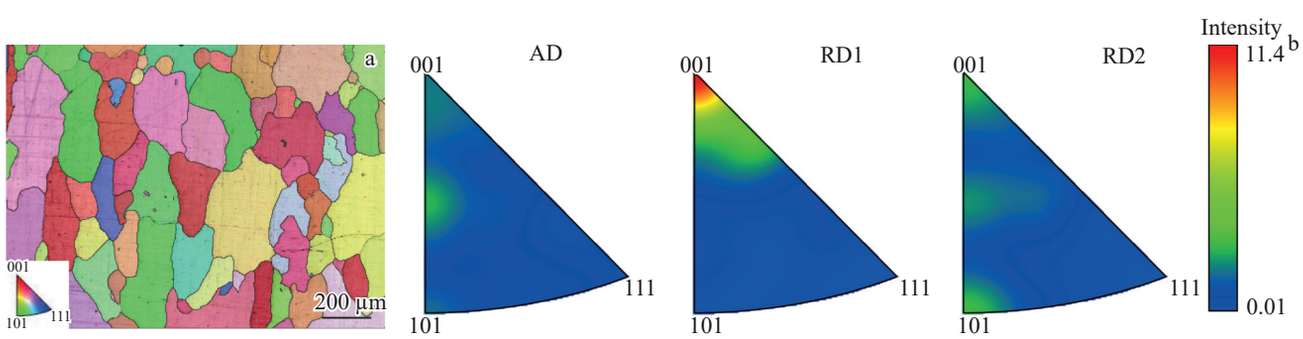

Fig.2 EBSD microstructure (a) and IPFs along different directions (b) of Pt before hot compression test

is attributed to the residual forging-induced anisotropy from annealing processing.

3.2 Stress-strain behavior

The true stress-true strain curves of the Pt under different temperatures and strain rates are displayed in Fig.3.

The true stress (i.e., flow stress) is increased significantly with the decrease in temperatures and the increase in strain rate, as illustrated in Fig. 3. During the initial stages of hot deformation, true stress rises sharply due to rapid generation and accumulation of dislocations. Dislocations produced during thermal deformation become entangled, restricting their mobility and forming work hardening areas[11]. The flow stress exhibits strong dependence on deformation temperature and strain rate. It can be seen that Pt demonstrates higher flow stress at low temperature under the same strain rate, though the flow stress difference between elevated strain rates decreases. Notably, the flow stress is decreased with the increase in temperature and the reduction in strain rate, because the thermal activation enables dynamic softening mechanisms, such as DRX and dynamic recovery (DRV), to counteract work hardening effect. Lower strain rate facilitates dislocation glide, suppressing dislocation multiplication and allowing more time for DRX and DRV to progress. At 873 and 923 K with the strain rate of 0.01 s^{-1}, these softening mechanisms dominate over work hardening, significantly reducing flow stress.

At high strain rates (1 – 10 s^{-1}), flow stress curves exhibit distinct behavior. When the strain rate is 1 s^{-1}, the flow stress curve shows multiple wavy patterns; whereas at strain rate of 10 s^{-1}, a single yield peak occurs at the initial stage of deformation (true strain of 0.18). This phenomenon arises from mobile dislocations concentrated at the grain boundaries. During deformation, boundary-impeded dislocation motion induces rapid accumulation, elevating flow stress abruptly. Once the dislocation density reaches a critical threshold, the pinned dislocations migrate inward from the grain boundaries, triggering abrupt DRV-driven stress reduction[12].

After the work hardening stage, higher strain rates lead to DRV, inducing partial strain softening. This phenomenon arises from dislocation density reduction through annihilation and recombination processes under elevated temperatures and low strain rates, thereby diminishing internal material stress[13]. Dynamic dislocation annihilation alleviates accumulated internal stress and partially counteracts work hardening effect. As deformation progresses, particularly at higher strains, the true stress undergoes minor oscillations after attaining a quasi-stable plateau. This result suggests a transition to the steady-state flow behavior, where DRV and work hardening reach dynamic equilibrium, as indicated by the true stress-true strain curves with strain rate of 1 and 10 s^{-1} in Fig.3c–3d.

3.3 Derivation of constitutive equation

During hot working, a characteristic energy barrier, namely deformation activation energy, should be surpassed, indicating that the hot processing is inherently a thermally activated process. The constitutive equation describes the influence of thermomechanical parameters, including strain rate, temperature, and strain, on flow stress during hot deformation[14]. This equation is widely applicable for accurately characterizing the high-temperature deformation behavior of metals.

The Zener-Hollomon parameter (Z), which correlates flow stress with key thermomechanical variables, is commonly

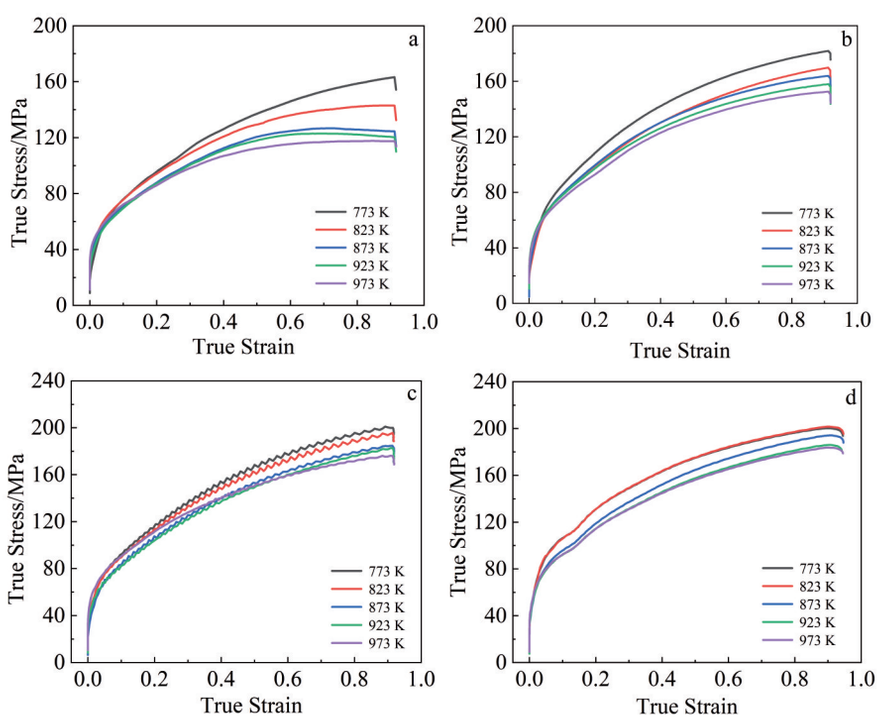

Fig.3 True stress-true strain curves of Pt under isothermal compression at different temperatures and strain rates: (a) 0.01 s^{-1}, (b) 0.1 s^{-1}, (c) 1 s^{-1}, and (d) 10 s^{-1}

expressed via Arrhenius-type equations. The exponential relationships governing low-stress and high-stress deformation regimes are defined by Eq.(1–2)[15], respectively, as follows:

$$Z = \dot{\varepsilon}\exp\left(\frac{Q}{RT}\right) = A_1\sigma_P^{n_1} \qquad \alpha\sigma_P \leqslant 0.8 \tag{1}$$

$$Z = \dot{\varepsilon}\exp\left(\frac{Q}{RT}\right) = A_2\exp\left(\beta\sigma_P\right) \qquad \alpha\sigma_P \geqslant 1.2 \tag{2}$$

where $\dot{\varepsilon}$ is strain rate; Q is apparent activation energy; R is gas constant; T is deformation temperature; A_1, A_2, n_1, α, and β are material parameters; σ_P is peak stress. This study employs a hyperbolic-sinusoidal Arrhenius-type equation to establish the constitutive relationship governing the thermal deformation of Pt. This equation is applicable across the entire stress range (for all stress conditions), which is expressed by Eq. (3), as follows:

$$Z = \dot{\varepsilon}\exp\left(\frac{Q}{RT}\right) = A\left[\sinh\left(\alpha\sigma_P\right)\right]^n \tag{3}$$

where A and n are the material constants. A can be obtained by the formula $\alpha = \beta/n_1$. Taking logarithms on both sides of Eq.(1–3), Eq.(4–6) can be obtained, respectively, as follows:

$$\ln\dot{\varepsilon} = n_1\ln\sigma_P + \ln A_1 - \frac{Q}{RT} \tag{4}$$

$$\ln\dot{\varepsilon} = \beta\sigma_P + \ln A_2 - \frac{Q}{RT} \tag{5}$$

$$\ln\dot{\varepsilon} = n\ln\left[\sinh\left(\alpha\sigma_P\right)\right] + \ln A - \frac{Q}{RT} \tag{6}$$

Using Eq.(4–6), the relationships of $\ln\dot{\varepsilon}$-$\ln\sigma_P$, $\ln\dot{\varepsilon}$-σ_P, and $\ln\dot{\varepsilon}$=$\ln\left[\sinh\left(\alpha\sigma_P\right)\right]$ can be obtained by linear fitting, as shown in Fig.4, and the corresponding slopes are the value of n_1, β, and n, respectively. Eq. (7) is derived by partially differentiating Eq.(6) with $\ln[\sinh(\alpha\sigma_P)]$ and $1/T$ as variables, as follows:

$$Q = Rn\left\{\frac{\partial\ln\left[\sinh\left(\alpha\sigma_P\right)\right]}{\partial\left(\frac{1}{T}\right)}\right\} \tag{7}$$

The apparent activation energy Q for hot deformation can be determined by the slope of the $\ln[\sinh(\alpha\sigma_P)]$-$1000/T$ curve (Fig. 4d). Q serves as a critical parameter for assessing the difficulty of thermal deformation, which is influenced by the peak stress σ_P and the stress index n. Q represents the minimum energy required for dislocation activation and slip during thermal deformation. Furthermore, Q exhibits a strong relationship between material composition and microstructure.

According to Eq.(3), the Z value under different strain rates and deformation temperatures can be obtained. Meanwhile, taking natural logarithm on both sides of Eq.(3), Eq.(8) can be obtained, as follows:

$$\ln Z = \ln A + n\ln\left[\sinh\left(\alpha\sigma_P\right)\right] \tag{8}$$

According to the relationship of $n\ln[\sinh(\alpha\sigma_P)]$-$\ln Z$, linear fitting is conducted, and the results are shown in Fig. 5. The intercept of the fitting line after regression is $\ln A$=10.109 47, so A=24 574.632 7.

These data are integrated with Eq. (3) to obtain the hyperbolic sinusoidal Arrhenius-type constitutive equation of Pt at peak strain level, as expressed by Eq.(9) as follows:

$$\dot{\varepsilon} = 24574.6327\left[\sinh\left(0.0063\sigma_P\right)\right]^{13.51265} \times\exp\left(-\frac{102.875}{RT}\right) \tag{9}$$

According to the constitutive equation and Eq.(9), the peak flow stress of Pt under different strain rates and deformation temperatures can be calculated, as expressed by Eq. (10), as

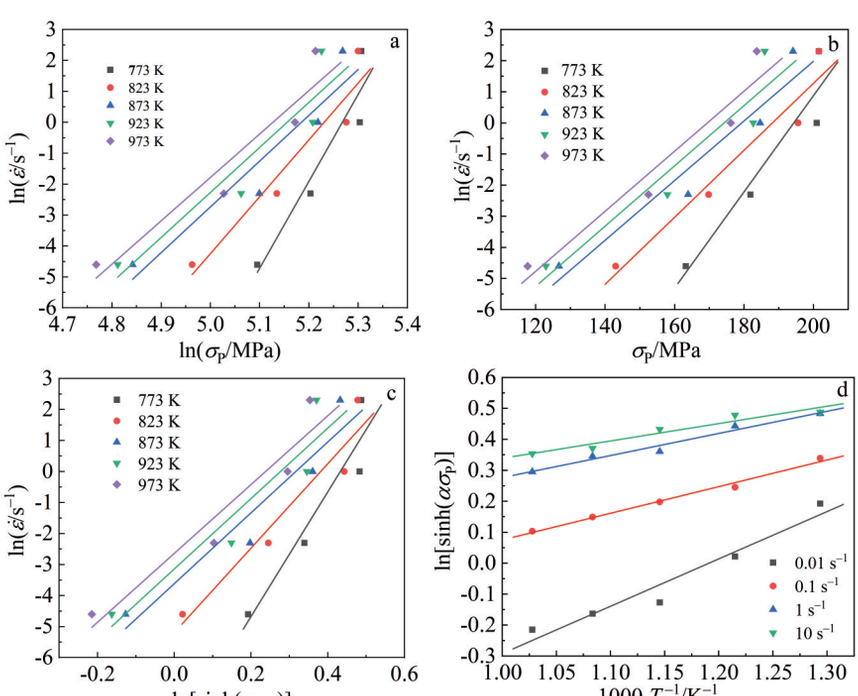

Fig.4 Relationships of $\ln\dot{\varepsilon}$-$\ln\sigma_P$ (a), $\ln\dot{\varepsilon}$-σ_P (b), $\ln\dot{\varepsilon}$-$\ln[\sinh(\alpha\sigma_P)]$ (c), and $\ln[\sinh(\alpha\sigma_P)]$-$1000/T$ (d) curves

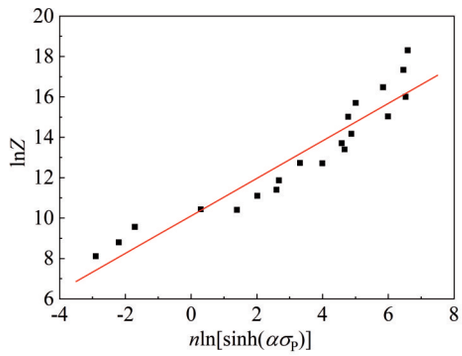

Fig.5 Variation of ln$Z$ with $n$ln[sinh($\alpha\sigma_P$)]

follows:

$$\sigma_P = \frac{1}{0.0063}\text{arcsinh}\{\exp[\frac{1}{13.51265}\times(\ln\frac{\dot{\varepsilon}}{24574.6327}+\frac{102.875}{RT})]\} \quad (10)$$

The value of the peak flow stress can be predicted, and the predicted peak flow stress is compared with the experimental peak flow stress, as shown in Fig.6.

As illustrated in Fig. 6, the peak flow stress predicted by Eq. (9) shows strong agreement with the experimental values under the test conditions. This validation confirms the predictive capability of the constitutive model. Furthermore, both experimental and predicted results demonstrate that the peak stress of Pt exhibits an inverse relationship with the deformation temperature, and it is increased monotonically with the increase in strain rate. This dependence highlights the significant influence of thermomechanical processing parameters on the flow behavior during hot deformation.

3.4 Establishment of processing map

The true stress-true strain curves of Pt obtained through thermal compression experiment not only characterize its high-temperature mechanical behavior, but also reveal the complex physical phenomena inherent to thermal deformation. To predict the flow behavior of Pt under elevated temperatures, a thermal processing map of Pt was established using these curves. The analysis employs the dynamic material model (DMM) framework[7], which uses mathematical modeling to describe thermomechanical parameters, such as strain rate, deformation temperature, and peak stress. Besides, the thermoplastic deformation processing can be optimized. Currently, DMM has been widely used to study the thermal deformation mechanism of various metals[16–17]. Its stability criteria, rooted in J-content and G-content calculations (J is related to the energy loss from microstructural evolution; G is the energy consumed in the plastic deformation stage), assume that the flow stress depends solely on strain rate, neglecting the direct strain dependence. This restriction may reduce the prediction accuracy for materials like titanium, where strain-dependent dynamic strain aging occurs during the cold/hot working[18]. It is noted that DMM can predict the instability regions for stainless steels[19], high-entropy alloys[20], Cu alloy[15], Mg alloy[21], and Ti alloy[22] in cold and hot working regions where the instabilities are predominant. In this study, DMM stability parameters, such as strain rate sensitivity of the flow stress, change rate of strain rate sensitivity, temperature sensitivity of flow stress, change rate of temperature sensitivity of flow stress with respect to strain rate, and activation energy, are used to identify the regions of instability.

According to the theory of DMM, a material is equivalent to a system of energy dissipation during thermal deformation, and this energy dissipation phenomenon is closely related to the rheological properties of materials. During processing, the energy dissipation is mainly achieved through two primary mechanisms: (1) G, representing the energy consumed in the plastic deformation stage, which is converted into heat energy and largely dissipated; (2) J, reflecting the energy losses from microstructure evolution, such as DRX, DRV, or superplastic deformation. The energy P absorbed in the unit area of the workpiece during thermal deformation is divided into dissipation energy G and dissipation covariance energy J, which can be expressed by Eq.(11)[16], as follows:

$$P = G + J = \int_0^{\dot{\varepsilon}} \sigma \mathrm{d}\dot{\varepsilon} + \int_0^{\sigma} \dot{\varepsilon} \mathrm{d}\sigma \quad (11)$$

where P is the total power of external force on the material; G is the energy consumed by the plastic deformation of the material (most of the energy is consumed in the form of heat, and a small part is stored in the form of defects); J is the energy consumed by the microstructure evolution during the deformation process of the material; m is the strain rate

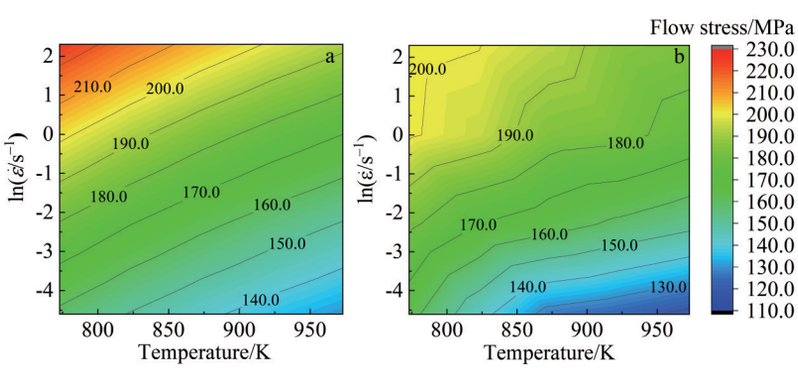

Fig.6 Predicted (a) and experimental (b) peak flow stress maps

sensitivity index. m value of the material has a relationship with G and J, as expressed by Eq.(12), as follows:

$$m = \frac{\partial J}{\partial G} = \frac{\dot{\varepsilon}\mathrm{d}\sigma}{\sigma\mathrm{d}\dot{\varepsilon}} = \frac{\partial \ln \sigma}{\partial \ln \dot{\varepsilon}} \tag{12}$$

Under ideal energy dissipation conditions (m=1), the dissipation of J will reach its peak, as denoted by $J_{max} = \sigma\dot{\varepsilon}/2$. However, during the actual thermoplastic deformation, materials deviate from this idealized state, exhibiting nonlinear energy dissipation behavior when the m value is between 0 and 1.

According to the theory of DMM, the constitutive relation of materials during thermoplastic deformation meets the following relationship:

$$\sigma = K\dot{\varepsilon}^m \tag{13}$$

where K is a related parameter. By substituting Eq. (13) into Eq.(11), Eq.(14) can be obtained:

$$J = \frac{m\sigma\dot{\varepsilon}}{m+1} \tag{14}$$

Based on $J_{max} = \sigma\dot{\varepsilon}/2$ and Eq. (14), a dimensionless parameter η, namely the power dissipation factor, can be obtained. This factor represents the ratio of energy dissipated during the microstructure evolution in the material forming process to the linearly dissipated energy. The expression of η is given in Eq.(15), as follows:

$$\eta = \frac{J}{J_{max}\frac{2m}{1+m}} \tag{15}$$

The power dissipation factor η is a key index that characterizes the relationship among deformation temperature, true strain, and strain rate, therefore being essential for the construction of hot processing maps. Once the true strain is determined, a contour map of the parameter η can be generated by plotting deformation temperature against the strain rate. Additionally, a power dissipation map can also be obtained. Factors affecting the value of η include DRV, DRX, internal fracture phenomena (cavity formation or wedge cracking), and the dissolution or coarsening of the second phases under dynamic deformation conditions. In the power dissipation map, regions with elevated η values typically indicate the higher dissipation capacity J, suggesting superior processing performance of the material under these conditions. However, comprehensive evaluation of the material processability necessitates integrating stability criteria and microstructural characterization to validate optimal processing windows.

Currently, numerous researchers have proposed various instability criteria based on the theory of DMM to predict defect formation domains during plastic processing, including the criteria developed by researchers Gegel, Malas, Prasad, and Murty. Among them, Prasad and Murty instability criteria are particularly prevalent in the studies of metal thermomechanical processing due to their simplicity and efficacy. Consequently, this study employed these two instability criteria to construct the instability map for Pt under thermal compression deformation.

Based on the principles of irreversible thermodynamics and Ziegler's principles of the maximum entropy production rate, the dissipation function D and the strain rate $\dot{\varepsilon}$ must satisfy the following inequality:

$$\frac{\mathrm{d}D}{\mathrm{d}\dot{\varepsilon}} < \frac{D}{\dot{\varepsilon}} \tag{16}$$

By substituting Eq. (16) into Eq. (14) and introducing the instability criterion ξ, Eq.(17) can be obtained, as follows:

$$\xi(\dot{\varepsilon}) = \frac{\partial \ln\left[m/(m+1)\right]}{\partial \ln \dot{\varepsilon}} + m \leqslant 0 \tag{17}$$

The instability criterion ξ serves as a quantitative indicator for assessing the deformation stability of materials under mechanical loading. This criterion integrates key processing parameters, such as stress, strain, temperature, and strain rate, to predict the transition from uniform deformation to localized instability phenomena, like shear band formation and crack initiation. When ξ<0, the material exhibits instability during high-temperature deformation, leading to the formation of localized shear bands with distinct deformation characteristics, compared with those of the surrounding matrix.

Nonetheless, the conventional formulation of the instability criterion ξ assumes a constant strain rate sensitivity factor m with respect to the strain rate $\dot{\varepsilon}$. This constitutive assumption restricts its applicability to materials conforming to the specific relationship. To overcome these constraints, researchers have developed generalized criteria with broader applicability. Thus, the Murty flow instability criterion incorporating m as a variable function has been proposed, as illustrated in Eq.(18), as follows:

$$2m < \eta \leqslant 0 \tag{18}$$

In this research, based on the complex constitutive behavior of Pt, the Murty instability criterion was selected to construct the instability diagram. Fig. 7c presents the resulting thermal processing diagram for Pt at the true strain of 0.9. This map integrates the experimental true stress-strain data with the power dissipation efficiency map (Fig. 7a) and plastic flow instability map (Fig. 7b). Within Fig. 7c, rheological instability domains are delineated by blue shading area, while safe processing windows are represented in white area. Contour lines denote the power dissipation coefficient (η) values. Notably, η values are consistently low (<0.20) under most deformation conditions, peaking at only 0.22. This suppression of η values, particularly pronounced at the areas with high strain rates (1 – 10 s^{-1}) and low temperature (773 – 823 K), and η values fall significantly below the values reported for other metals under comparable thermomechanical processing[19,23]. This observation is attributed to the relatively low maximum temperature (973 K) achieved in the hot compression tests.

The processing map in Fig. 7c reveals three distinct instability domains. These domains correspond to deformation conditions characterized by low temperature (773 K) coupled with a low strain rate (0.01 s^{-1}), moderate temperature (823 K) coupled with low-to-intermediate strain rates (0.01 and 0.1 s^{-1}), and elevated temperature (873 K) coupled with high strain rates (1 and 10 s^{-1}). Conversely, all other test thermomechanical conditions are related to the stable

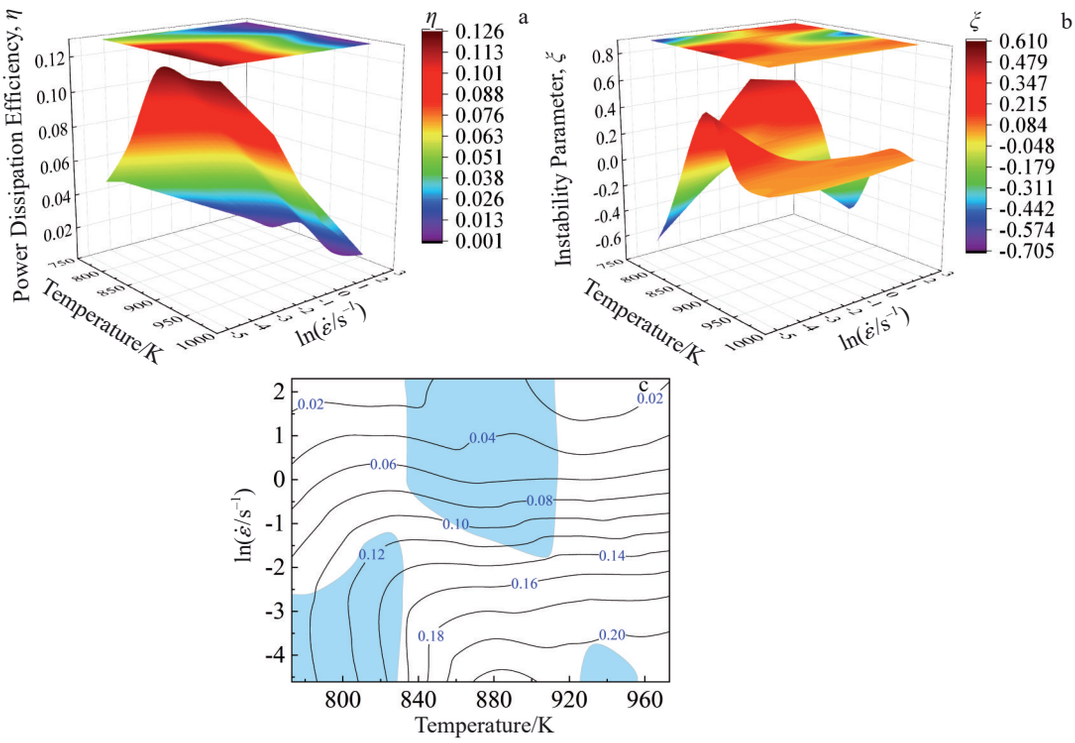

Fig.7 Power dissipation efficiency map (a), plastic flow instability map (b), and thermal processing map (c) of Pt under true strain of 0.9

processing regions.

3.5 Microstructure evolution based on processing map domains

To validate the instability and stability domains in the hot processing map of Pt at true stress of 0.9 (Fig. 7c), the microstructure characterization was performed on the representative key regions of deformed samples. Fig. 8 presents IPFs of the microstructure evolution under different thermomechanical conditions.

EBSD analysis quantified DRX rate and grain size of Pt at different temperatures and strain rates, as presented in Fig.9.

A notable inverse correlation exists between DRX kinetics and grain size. Fig. 9a identifies the maximum DRX rate (19.0%) under conditions of 873 K and 0.01 s^{-1}, while Fig.9b reveals that coarser grains predominantly exist under the low-strain-rate and high-temperature conditions. Under the conditions of low temperature (773 K) and high strain rate (10 s^{-1}), restricted DRX coupled with grain fragmentation and subgrain formation yields refined grains. Insufficient driving force for grain boundary migration restricts grain growth after nucleation at high deformation temperature and low strain rate (973 K, 0.01 s^{-1}). The samples under the conditions within instability regions (873 K, 10 s^{-1}; 773 K, 0.01 s^{-1}) exhibit anomalous grain coarsening despite negligible DRX (<0.5%), which is attributed to localized deformation induced boundary migration. Conversely, grain growth at 873 K with strain rate of 0.01 s^{-1} is DRX-dominated. These microstructural observations align with the flow softening behavior in Fig.3a, confirming DRX as the primary softening mechanism at 873–923 K.

To elucidate the substructural evolution of Pt under varying deformation conditions, transmission electron microscopy (TEM) analysis was performed on samples deformed at 873 K. At this temperature, Pt exhibits complex microstructural behavior across four representative strain rates (0.01, 0.1, 1, and 10 s^{-1}). This targeted characterization resolves deformation mechanisms inaccessible via EBSD, particularly the dislocation configurations and subgrain formation. TEM images of the sample deformed under different strain rates are presented in Fig.10.

The microstructure evolution of Pt at 873 K exhibits pronounced strain-rate dependency. This behavior governs the stability transition observed in processing map analysis (Fig. 7c), where increasing strain rate from quasi-static state (0.01 s^{-1}) to severe state (10 s^{-1}) shifts the deformation response from stable processing domains to thermomechanical instable regimes. Under quasi-static deformation (0.01 s^{-1}), extensive DRX occurs, which is characterized by equiaxed grain growth with well-defined boundaries and substantial dislocation density reduction (Fig. 10a). This phenomenon results from dislocation consumption during recrystallization.

At intermediate strain rate (0.1 s^{-1}), transitional microstructures, localized DRX nucleation, coexisting dislocation tangles, and subgrains exist (Fig. 10b). In this research, accelerated dislocation formation surpasses DRV kinetics, promoting subgrain formation while restricting the recrystallization. Conversely, high strain rates (1 and 10 s^{-1}) induce microstructural instability manifested through

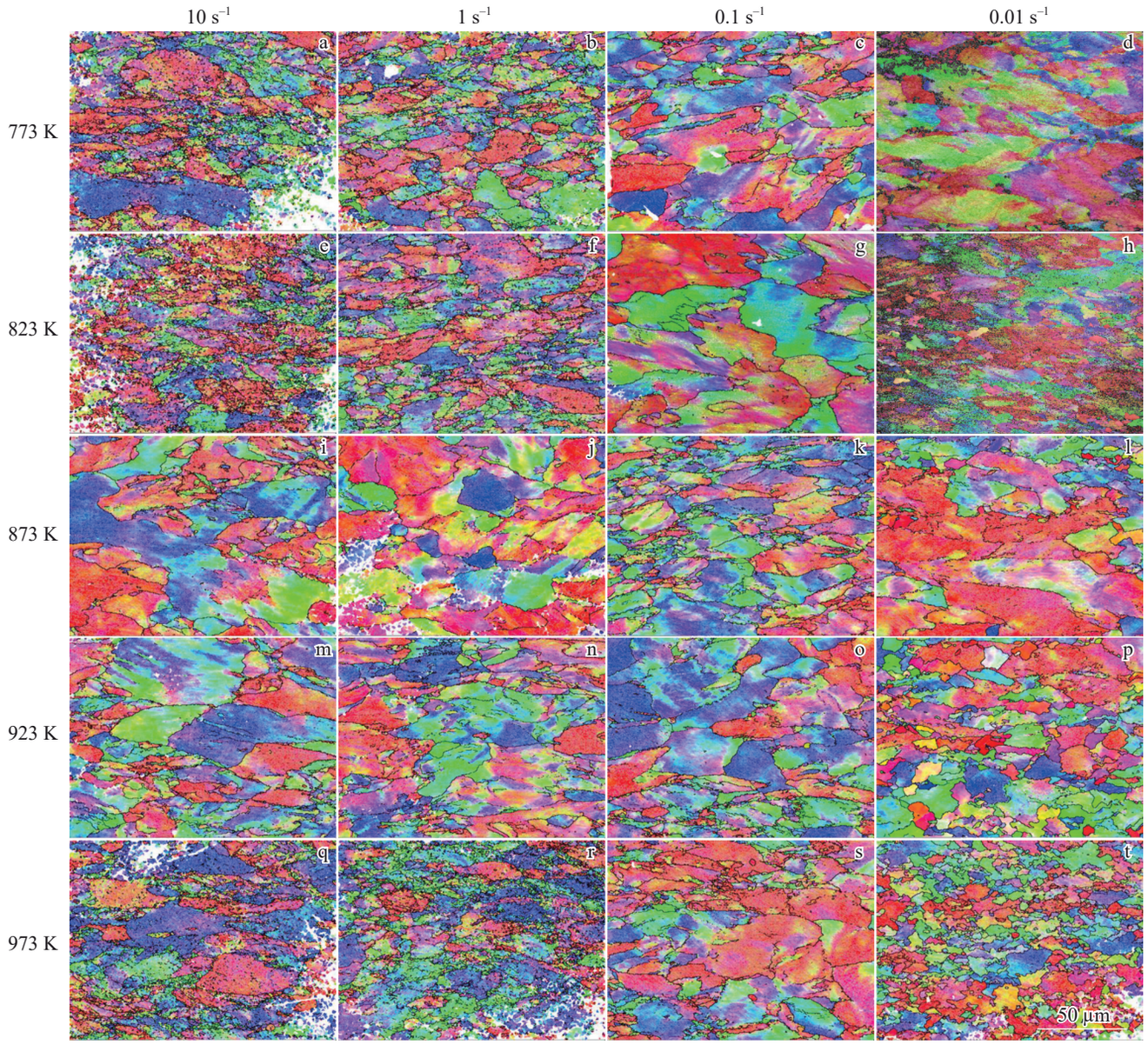

Fig.8 IPFs of microstructures of Pt at true strain of 0.9 under different temperatures and strain rates

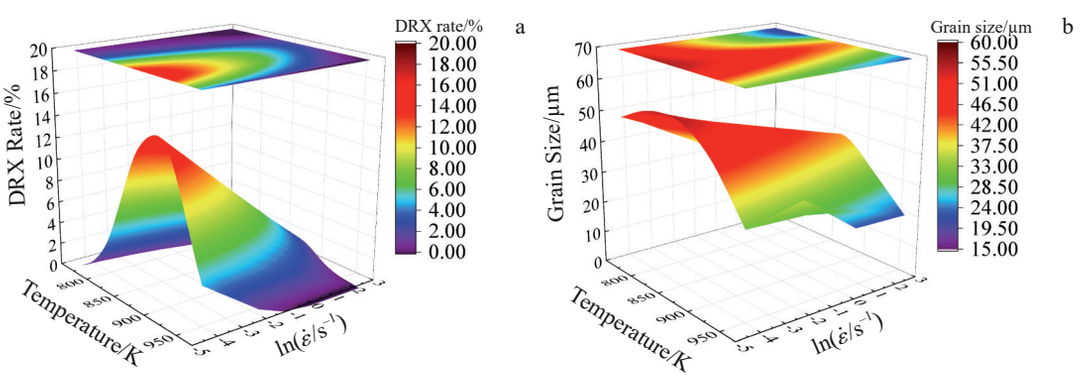

Fig.9 DRX rate (a) and grain size (b) of Pt constructed with strain of 0.9 at different temperatures and strain rates

heterogeneous grain size distribution, deformation banding, and diffuse subgrain boundaries (Fig.10c–10d), indicating the shear localization. These microstructures exhibit elevated dislocation densities without DRX nucleation, confirming the dominance of dislocation slip. The reduced deformation duration restricts the recrystallization, while the dislocation-modified matrix is cut, generating refined subgrains. Local strain concentration concurrently facilitates anomalous grain

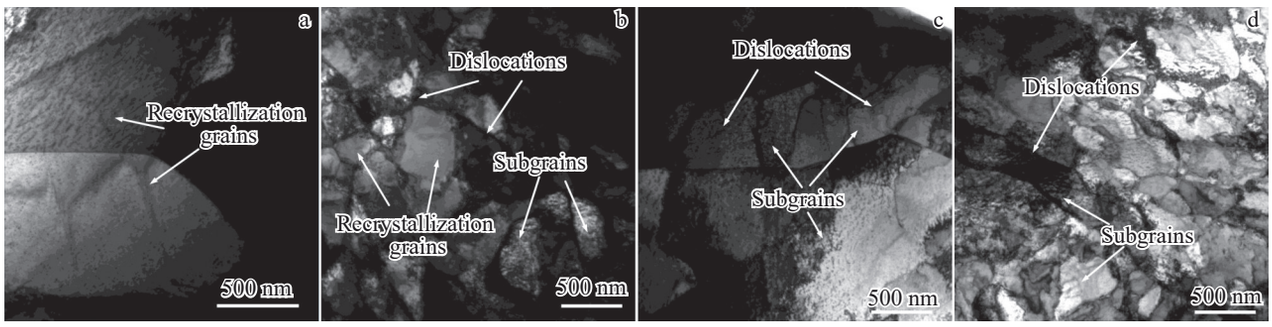

Fig.10 TEM images of samples deformed at 873 K and different strain rates: (a) 0.01 s^{-1}, (b) 0.1 s^{-1}, (c) 1 s^{-1}, and (d) 10 s^{-1}

coarsening. This process directly corresponds to unstable domains in the hot processing map of Pt.

The established Arrhenius-type constitutive equation reveals distinctive deformation characteristics of Pt. The activation energy for deformation (Q=102.875 kJ/mol) is significantly lower than the activation energy for self-diffusion (approximately 257 kJ/mol) [24], indicating the contribution of non-thermally activated mechanisms, such as grain boundary sliding or dislocation climb, to plastic flow during hot deformation. The exceptionally high strain rate sensitivity exponent (n=13.5), compared with the typical values for metals (3 – 8) [5,25], underscores the extreme sensitivity of Pt to strain rate and temperature variations[26]. This sensitivity correlates directly with the stress drop observed at high strain rates (strain rate of 10 s^{-1} in Fig. 3), reflecting intense competition between dislocation multiplication and DRV. The hot processing map further clarifies microstructure evolution patterns. The low power dissipation efficiency (η <0.22), which is substantially lower than the typical values (η >0.30) for metal materials (such as titanium alloys) [7], indicates that energy dissipation in Pt is dominated by heat generation (G), and a small amount of energy is consumed by microstructure transformation (J). This observation aligns with the low maximum DRX fraction of only 19.0% (Fig. 9a), confirming the weak intrinsic recrystallization driving force. Application of the Murty instability criterion ($2m$< η) effectively identifies the unstable processing regions (773 K, 0.01 s^{-1}; 873 K, 10 s^{-1}). The localized shear bands, abnormal grain growth (Fig. 10c), and microcracks[27] all indicate the unstable microstructure of Pt, and they are caused by the stress concentrations induced by grain boundary sliding and adiabatic shear resulting from thermal softening due to rapid plastic work conversion.

According to previous research, the interaction between microstructure evolution and mechanical response is mainly manifested in two mechanisms, DRX-dominated flow softening and dislocation evolution-dominated strengthening. Within the optimal processing window (860 – 910 K, 0.01 – 0.1 s^{-1}), DRX, a critical restoration mechanism involving nucleation and boundary migration of strain-free grains[28], significantly reduces flow stress (Fig. 3a) by consuming stored deformation energy. This process consists of an efficient power dissipation pathway[29], converting mechanical energy into microstructural reorganization while mitigating stress localization. DRX kinetics in Pt exhibits strong thermomechanical dependence: elevated strain rates increase stored energy and nucleation driving force but constrain the growth kinetics. Besides, the reduced strain rates (≤0.1 s^{-1}) facilitate boundary migration and grain coarsening. Increasing the temperature reduces activation barrier for dislocation mobility and accelerates diffusion-modified boundary migration based on $D_{gb}=D_0\exp(-Q_{gb}/RT)$ [21,30], where D_{gb} is dissipation of grain boundary, D_0 is initial dissipation, and Q_{gb} is activation energy of grain boundary. These phenomena enhance both the nucleation kinetics and growth kinetics. Consequently, the intermediate regime (873–923 K, 0.01–0.1 s^{-1}) provides optimal thermal activation and sufficient growth time for DRX, yielding uniform equiaxed grains (Fig. 10a), eliminating the initial <001> texture (Fig. 2b), and thereby improving the formation uniformity. At high strain rates (10 s^{-1}), rapid dislocation formation (Fig. 10d) causes pronounced work hardening. Subsequent stress reduction stems from dislocation rearrangement into subgrains (DRV mechanism). Notably, the grain refinement (reducing the grain size to approximately 20 μm) at 773 K and 10 s^{-1} (Fig. 9b) coincides with the increased flow stress (Fig. 3d), demonstrating that the strengthening contribution from elevated dislocation density (ρ) outweighs the Hall-Petch effect. This result is consistent with the fundamental dominance of dislocation strengthening on deformation resistance.

This study investigated the hot processing map of Pt through the multiscale characterization. However, the lack of quantification of performance indicators, such as hardness and electrical conductivity, restricts the direct correlation between microstructure and performance. In the future, it is necessary to combine microstructure with alloy design to continuously optimize the microstructure control strategy for high-temperature processing of Pt alloys.

4 Conclusions

1) The predicted peak stress is basically consistent with the experimental result. The peak flow stress is decreased with the increase in temperature and the decrease in strain rate, indicating a high sensitivity of flow stress to deformation temperature and strain rate.

2) Using the modified flow stress data, a hyperbolic sine

Arrhenius-type constitutive equation for the peak strain prediction of Pt is obtained:

$$\dot{\varepsilon} = 24574.6327\left[\sinh\left(0.0063\sigma_{\mathrm{P}}\right)\right]^{13.51265}\exp\left(-\frac{102.875}{RT}\right).$$

The relationship between flow stress during deformation and thermal deformation parameters can be accurately predicted by the constitutive equation.

3) The optimal processing window lies within 860–910 K and 0.01–0.1 s^{-1}, which is characterized by fine homogeneous grains, low deformation resistance, and enhanced plasticity.

4) The softening of Pt at 873 and 923 K is primarily due to DRX.

References

1 Okamoto H. *Journal of Phase Equilibria and Diffusion*[J], 2013, 34(2): 176
2 Hu J Y, Xu J Y, Feng R *et al*. *Nano Today*[J], 2024, 59: 102543
3 Hill P J, Cornish L A, Fairbank J B. *JOM*[J], 2001, 53(10): 19
4 Zhang M X, Zhang B J, Jiao X Y *et al*. *Materials Characterization*[J], 2024, 211: 113915
5 Jiang J F, Xu S Y, Liu S H *et al*. *Journal of Alloys and Compounds*[J], 2025, 1010: 177312
6 Yan Y, Luo D, Wu W *et al*. *Journal of Alloys and Compounds*[J], 2024, 1007: 176442
7 Chai Y P, Zhu Y C, Qin L *et al*. *Materials Today Communications*[J], 2024, 41: 110599
8 Yu J X, Li Z J, Qian C *et al*. *Journal of Materials Research and Technology*[J], 2023, 23: 2275
9 Deng L, Tian Z, Hao Y *et al*. *International Journal of Hydrogen Energy*[J], 2024, 50(Part B): 784
10 Liu L, Zhou Z J, Yu J *et al*. *Acta Metallurgica Sinica* (*English Letters*)[J], 2024, 37(8): 1453
11 Fu C Z, Tao C C, Huang H J *et al*. *Intermetallics*[J], 2024, 171: 108342
12 Zhou X, Fu L, Cheng J *et al*. *Materials Letters*[J], 2023, 342: 134326
13 Yang Y, Wang H, Feng Z Q *et al*. *Journal of Materials Research and Technology*[J], 2024, 33: 8929
14 Tao C C, Zhou G, Huang H J *et al*. *Materials Characterization*[J], 2024, 208: 113673
15 Mirahmadi D, Dehghani K, Shamsipur A *et al*. *Journal of Materials Research and Technology*[J], 2023, 24: 376
16 Zhao Q, Yu L M, Ma Z Q *et al*. *Materials*[J], 2018, 11(6): 1044
17 Ma Z, Shu X D, Xu H J *et al*. *Journal of Alloys and Compounds*[J], 2024, 1002: 175282
18 Venugopal S, Venugopal P, Mannan S L, *Journal of Materials Processing Technology*[J], 2008, 202(1–3): 201
19 Samantaray D, Mandal S, Bhaduri A K, *Materials Science and Engineering A*[J], 2011, 528(15): 5204
20 Jiang J F, Huang M J, Wang Y *et al*. *Journal of Alloys and Compounds*[J], 2021, 876: 160102
21 Liu Q B, Luan S Y, Liu X Y *et al*. *Materials Today Communications*[J], 2024, 39: 109154
22 Chen Y J, Su H, Zhao Z *et al*. *Materials Today Communications*[J], 2024, 39: 109075
23 Zhang J Q, Di H S, Mao K *et al*. *Materials Science and Engineering A*[J], 2013, 587: 110
24 Mehrer H. *Diffusion in Solids*[M]. Berlin: Springer, 2007: 297
25 Zhang Y S, Jiang X Y, Zhou G *et al*. *Rare Metal Materials and Engineering*[J], 2024, 53(1): 38
26 Wang X J, Yang J Z, Wang S C *et al*. *Rare Metal Materials and Engineering*[J], 2024, 53(10): 2891
27 Yao J L, Zhang D, Zhang J S. *Rare Metal Materials and Engineering*[J], 2022, 51(6): 2046
28 Liu M, Shan Z D, Li X Y *et al*. *Journal of Materials Research and Technology*[J], 2023, 24: 724
29 Xu H J, Hu W Q, Kang C *et al*. *ISIJ International*[J], 2021, 61(3): 967
30 Ling K, Mo W F, Deng P *et al*. *Materials Today Communications*[J], 2023, 34: 105300

铂的热变形行为及显微组织演变

唐会毅[1,2,3]，栾佰峰[1]，张夫恩[1]，肖雨辰[2,3]，柴林江[4]，吴保安[2,3]

(1. 重庆大学 材料科学与工程学院 教育部轻合金材料国际合作联合实验室，重庆 400045)

(2. 重庆材料研究院有限公司，重庆 400707)

(3. 国家仪表功能材料工程技术研究中心，重庆 400707)

(4. 重庆理工大学 材料科学与工程学院，重庆 400054)

摘　要：通过热压缩实验研究了铂的热变形行为，通过对应力-应变曲线的分析，构建了预测铂流动特性的本构方程。利用本构方程，计算了不同温度和应变速率下铂在热加工过程中的峰值应力。结果表明：预测值与实验结果非常吻合。电子背散射衍射分析揭示了安全加工区域内不同条件下的热变形机制。优选的加工参数为变形温度860~910 K，应变速率0.01~0.1 s^{-1}。在高应变速率下观察到的不连续屈服是由于晶界上可动位错的增殖和运动造成的。

关键词：铂；微观结构演化；热变形；加工图；应变率

作者简介：唐会毅，男，1983年生，硕士，正高级工程师，重庆大学材料科学与工程学院教育部轻合金材料国际合作联合实验室，重庆 400045，E-mail：hytang320@163.com